The Trails of Superluminal Jet Components in 3C 111

M. Kadler[1,2], E. Ros[2], M. Perucho[2], Y. Y. Kovalev[2,3], D. C. Homan[4], I. Agudo[2,5], K. I. Kellermann[6], M. F. Aller[7], H. D. Aller[7], M. L. Lister[8], and J. A. Zensus[2]

Received _____; accepted _____

[1]NASA Postdoctoral Research Associate; Astrophysics Science Division, NASA's Goddard Space Flight Center, Greenbelt Road, Greenbelt, MD 20771, USA; Matthias.Kadler@nasa.gov

[2]Max-Planck-Institut für Radioastronomie Bonn, Auf dem Hügel 69, 53121 Bonn, Germany; ros, perucho, ykovalev, azensus@mpifr-bonn.mpg.de

[3]Astro Space Center of Lebedev Physical Institute, Profsoyuznaya 84/32, 117997 Moscow, Russia; ykovalev@mpifr-bonn.mpg.de

[4]Astronomy Department, Department of Physics and Astronomy, Denison University, Granville, OH 43023, U.S.A.; homand@denison.edu

[5]Instituto de Astrofisica de Andalucia, Dept. de Radioastronomia y Estructura Galactica, C/Camino Bajo de Huetor, 50, 18008 Granada, Spain; iagudo@iaa.es

[6]National Radio Astronomy Observatory, 520 Edgemont Road, Charlottesville, VA 22903, U.S.A; kkellerm@nrao.edu

[7]Astronomy Department, University of Michigan, Ann Arbor, MI 48109-1042, U.S.A.; mfa, haller@umich.edu

[8]Department of Physics, Purdue University, 525 Northwestern Avenue, West Lafayette, IN 47907, U.S.A.; mlister@physics.purdue.edu

ABSTRACT

The parsec-scale radio jet of the broad-line radio galaxy 3C 111 has been monitored since 1995 as part of the 2 cm Survey and MOJAVE monitoring observations conducted with the VLBA. Here, we present results from 18 epochs of VLBA observations of 3C 111 and from 18 years of radio flux density monitoring observations conducted at the University of Michigan. A major radio flux-density outburst of 3C 111 occured in 1996 and was followed by a particularly bright plasma ejection associated with a superluminal jet component. This major event allows us to study a variety of processes associated with outbursts of radio-loud AGN in much greater detail than possible in other cases: the primary perturbation gives rise to teh formation of a forward and a backward-shock, which both evolve in characteristically different ways and allow us to draw conclusions about the workflow of jet-production events; the expansion, acceleration and recollimation of the ejected jet plasma in an environment with steep pressure and density gradients are revealed; trailing components are formed in the wake of the primary perturbation as a result of Kelvin- Helmholtz instabilities from the interaction of the jet with the external medium. The jet-medium interaction is further scrutinized by the linear-polarization signature of jet components traveling along the jet and passing a region of steep pressure/density gradients.

Subject headings: galaxies: individual: 3C111 – galaxies: active – galaxies: jets – galaxies: nuclei

1. Introduction

The VLBA 2 cm Survey (Kellermann et al. 1998; Zensus et al. 2002; Kellermann et al. 2004; Kovalev et al. 2005) and its follow-up program MOJAVE[1] (Lister & Homan 2005) have provided an unprecedented data base of outflow dynamics in radio jets ejected from quasars and active galaxies. Measured jet speeds and polarization dynamics of hundreds of extragalactic jets in this project, allows us to address global questions about the effects of relativistic beaming and the intrinsic properties of extragalactic radio jets (Cohen et al. 2007), their intrinsic brightness temperatures (Homan et al. 2006) or their Lorentz factor distribution and luminosity function (Kellermann et al. 2004; Cara & Lister 2007).

Complementary to this *global approach*, the VLBA 2 cm Survey/MOJAVE data base holds high-quality multi-epoch information about the (sub-)parsec scale structure of the jets of hundreds of individual objects both in total intensity and in polarization. Here, we report the results from ten years of Very-Long-Baseline Interferometric (VLBI) observations of 3C 111 as part of the VLBA 2 cm Survey and MOJAVE programs. We scrutinize the parsec-scale source structure during a major flux-density outburst and during its aftermath.

The nearby (z=0.049)[2] broad-line radio galaxy 3C 111 (PKS B 0415+379) shows a classical FR II morphology on kiloparsec-scales spanning more than 200″ with a highly collimated jet connecting the central core and the northeastern lobe in position angle 63° while no counterjet is observed towards the southwestern lobe (Linfield & Perley 1984). This asymmetry, which is usually explained via relativistic boosting of the jet and de-boosting of the counter-jet, is even more pronounced on parsec-scales: 3C 111 exhibits

---

[1] `http://www.physics.purdue.edu/MOJAVE`

[2] Assuming a Hubble constant of $H_0 = 71\,\mathrm{km\,s^{-1}\,Mpc^{-1}}$, $\Omega_\mathrm{M} = 0.3$, $\Omega_\Lambda = 0.7$, this results to a linear scale of $1.0\,\mathrm{pc\,mas^{-1}}$.

the brightest compact radio core at cm/mm wavelengths of all FR II radio galaxies. It was the first lobe-dominated extragalactic radio source in which superluminal motion was detected (Goetz et al. 1987; Preuss, Alef, & Kellermann 1988). High-radio-frequency VLBI data of 3C 111 have been reported on by Alef et al. (1998) and Kharb et al. (2003).

In Sect. 2, the VLBA 2 cm Survey observations and the data reduction are described. Observational results are presented in Sect. 3. In Sect. 4, we discuss the various observed processes at work as the plasma injected into the jet as a result of the outburst is traveling downstream along the jet. In Sect. 5, we put these results into the context of future simulations and observations with the goal of understanding the production mechanisms of AGN jets.

2. Observations and data analysis

3C 111 has been monitored as part of the VLBA 2 cm Survey program since April 1995. The observational details are given by Kellermann et al. (1998). Following the methods described there, the data from 17 epochs of VLBA 2 cm Survey observations of 3C 111 between 1995 and 2005 (see Table 1) were phase and amplitude self calibrated and the brightness distribution was determined via hybrid mapping. An additional epoch from June 2000 was added from an independent program (PI: G. Taylor). Two dimensional Gaussian components were fitted in the (u, v)-domain to the fully calibrated visibility data of each epoch using the program DIFMAP. The parameters of the various model fits at the various epochs are given in Table 5. The models were aligned at the various epochs by assuming the westernmost component (namely, the "core") to be stationary so that the position of jet components can be measured relative to it. Because of the coupling of the flux densities of nearby model components, the true flux-density errors are larger than the formal (statistical) errors in most cases (unless the given model component is far enough

separated from its closest neighbor). Throughout this paper, conservative errors of 15 % are assumed for the flux densities of individual model-fit components. Positions uncertainties were determined internally from the deviations of the data from linear motion.

3. Results

3.1. The 1996 Radio Outburst of 3C 111

A strong flux density outburst of 3C 111 occurred in 1996, which was first visible in the mm band and some months later at lower radio frequencies. In fact, this outburst was first detected at 90 GHz with the IRAM interferometer at Plateau de Bure in January 1996 with flux densities > 10 Jy (Alef et al. 1998), at 37 GHz in March 1996, and at 22 GHz in August 1996 (Teräsranta et al. 2004). Figure 1 shows the single-dish radio light curves of 3C 111 at 4.8 GHz, 8 GHz, and 14.5 GHz obtained from the UMRAO radio-flux-density monitoring program (Aller, Aller, & Hughes 2003). These data show that from early 1996 on the radio-flux density of 3C 111 was rising at 14.5 GHz, reaching its maximum in late 1996. At the two lower frequencies, the flux-density maximum was reached at subsequent later times, in mid 1997 at 8 GHz and in late 1997 at 4.8 GHz. The profile of the outburst in the flux-density vs. time domain shows a narrow, high-amplitude peak between early 1996 and late 1997, which is almost symmetric. After late 1997, a slower-decreasing tail component dominates the light curves, most clearly visible at 14.5 GHz.

The flare propagated through the spectrum as qualitatively expected by standard jet theory with the high-frequency radio emission coming from the most compact regions of the jet and the emission peak shifting to lower frequencies as a newly ejected jet component travels down the jet becoming optically thin. The shift rate with frequency is ~ 10 GHz/yr.

The evolution of the spectral index α for 14.5/8.0 GHz and 8.0/4.8 GHz is shown in

Fig. 2. Before 1996, the sampling is too sparse to derive a continuous course of the spectral index in the 14.5/8.0 GHz band. Between, 8.0 GHz and 4.8 GHz, the spectral index is ~ -0.7 for the pre-1996 period. The radio flux-density outburst in 1996 went along with a subsequent flattening of the spectrum with a maximum value of $\alpha \sim 0$ in the 14.5/8.0 GHz band reached in mid 1996. In the post-outburst period between 1998 and 2004 α is typically in the range -0.5 to -0.7 between 14.5 GHz and 8.0 GHz and slightly steeper (-0.7 to -0.9) in the 8.0/4.8 GHz band. The overall steeper spectral index at lower frequencies can be understood as the contribution of optically thin large-scale emission from the radio lobes of 3C 111 to these single-dish light curves.

3.2. VLBA Monitoring Results

Figure 3 shows the variable parsec-scale structure of 3C 111 at 18 different epochs of VLBA 2 cm Survey and MOJAVE observations between 1995.27 and 2005.73. The variable source structure can be described by a classical one-sided core-jet morphology in the first two epochs with typical velocities of the outward moving jet components of $\sim 1.4 - 1.7\,\mathrm{mas\,yr^{-1}}$ corresponding to $\sim 5\,c$. In 1996.82 a new jet component, even brighter than the core, dominates the source structure. By 1997.19, this new component has got even brighter (~ 3.4 Jy) and in the following epochs it travels along the jet while it becomes gradually more stretched out along the jet-ridge line.

Model Fitting: In Fig. 4 the radial distance of the various model fit components from the core is shown as a function of time. Position uncertainties have been determined from the internal deviations of the data from linear motions for each component[3]. The component

[3]Note that the errors for E 1 have been determined separately for the pre-2004 and post-2004 epochs because of the partial resolution of this component after 2004. Note also that

identification was conducted, based on a comparison of the positions and flux densities, and a linear regression of the core distances as a function of time was performed to determine the kinematics. The derived component velocities are tabulated in Table 3. The early outer jet components (A, B, C, D) of the 1995.27 epoch can be traced over two to four epochs before their flux densities fall below the detection threshold (compare Fig. 5). In late 1996 and early 1997, the source structure is dominated by the emission of the core and the newly formed jet components E and F, with E being the leading component. The two components travel outwards with a mean apparent velocity of $(1.00 \pm 0.02)\,\mathrm{mas\,yr^{-1}}$ and $(0.64 \pm 0.07)\,\mathrm{mas\,yr^{-1}}$, respectively. Before mid 1997, component F is substantially brighter than component E but after that, its flux density is dropping steeply. F is not detected any more after 1998.18 while E is still $\sim 800\,\mathrm{mJy}$ bright at that time. The light curves of E and F reproduce qualitatively the two-component shape of the flux-density outburst in Fig. 1 with component F being responsible for the narrower and higher-amplitude peak between early 1996 and late 1997 and component E dominating the slower-decreasing tail of the outburst after late 1997 (compare Fig. 5 and discussion below). In the following epochs E splits into four distinct components (E1, E2, E3, E4). This takes place at distances of 3.5–4.5 mas from the core. E2, E3, and E4 move all at subsequently slower speeds than E1, resulting in an elongated morphological structure of the associated emission complex.

In later epochs, new components are ejected from the core into the jet. The two strongest of them (G,H) can be traced through the following eight and nine monitoring epochs, respectively. Component H splits into three individual components in 2004.27 and a fourth associated component is seen from 2004.80 on. In the following, we refer to the components E1, and H1 as the "leading components" and to E2, E3, E4, H2, H3, and

---

errors for components with less than three epochs were estimated from other components at similar positions in the jet and with similar flux densities.

H 4 as the "trailing components" of E and H, respectively.

From the linear-regression, ejection epochs of the individual jet components can be determined by back-extrapolating the component trajectories to the core. In Fig. 1, these ejection epochs and the associated uncertainties are indicated as shaded areas. It is apparent that the ejection of the components E and F coincides with the onset of the major flux-density outburst in 1996 described above. The following major component ejections (G, H, and the combined M/N event) all have direct counterparts in local maxima of the radio light curve, especially at 14.5 GHz. Fig. 2 shows that all these ejection epochs coincide with local maxima of the spectral index in the 14.5/8.0 GHz band. Between 2002 and 2004, a number of minor component ejections took place but the regression-fit quality (due to the closeby components, the low flux densities and the small time baseline) does only moderatly constrain the ejection epochs. In addition, the time sampling of UMRAO observations in this time range is relatively poor, in particular from mid 2001 to mid 2003.

Flux Density Evolution: Figure 5 shows the brightness evolution of the core and the jet components that have been ejected prior to 2001.50 with time. Apparently, the trailing components E 4 and H 4 appear first in a rising state, i.e., they first increase in flux before they become fainter in later epochs. Component F shows an extraordinary steep decrease in brightness in 1997–1998. As mentioned before, not the leading component E but the following component F dominated the light curve in the first year after the outburst. In Fig. 6 and Fig. 7, the flux-density evolution of the components E, G, and H and the associated leading and trailing components are shown with traveled distance from the core, respectively. To display a blended flux-density evolution for the full component E ejection region after it split up into the four distinct components, the flux densities of E 1, E 2, E 3, and E 4 were added for the post-1999 epochs and a flux-density weighted effective position was calculated for the blended feature that would be visible at lower resolution.

The ejecta first rise in flux density within the inner 1 mas from the core, then there is a decline about three orders of magnitude in the following decade, exhibiting a plateau or broad local maximum in 1998–2000 at a distance from 3–5 mas from the core. Component H and its leading and trailing components exhibit a similar behavior although on about an order of magnitude lower flux-density levels. It is interesting to note that component G, although it does not appear to split into leading and trailing components like E and H, does exhibit a pronounced flux density maximum after 2002, as well, approximately at the same distance from the core where the trailing components of E and H are originated. It is further noteworthy that G catches up to E 4 in 2004.27 and that both components are represented through a blended two-component model in this epoch. The relatively high measured flux density of E 4 in this epoch may be an effect of imperfect decomposition of the blended emission region.

The T_b gradient along the jet: Following Kadler et al. (2004); Kadler (2005), the brightness temperature gradient s can be parametrized as

$$s = l + n + b(1 - \alpha) \tag{1}$$

where l, n and b are the power law indices that describe the gradients of jet diameter d, particle density n_e, and magnetic field B with core distance r. Conservation of magnetic energy along the jet implies a constant energy partition along the jet

$$B^2 \propto n_e, \Rightarrow b = n/2 \quad . \tag{2}$$

With $\alpha = -0.5$, it follows

$$s = l + 7/4\, n \tag{3}$$

Figure 8 shows the brightness temperatures of all jet components in the parsec-scale jet of 3C 111 at 2 cm wavelength between 1995 and 2005 as a function of their core distance. In

general, the brightness temperature of all components decreases as the components travel outwards but an approximation with a simple power law does not yield a good fit to the full data set ($\chi^2 = 1.8$, 115 d.o.f.). Visual inspection of Fig. 8 shows that this is due to the E–, F– and H– components, in particular after splitting up into sets of leading and trailing components. This behavior is different than expected for a straight and stable jet geometry in which the power-law dependences of the particle density, the magnetic field strength and the jet diameter on the core distance predicts that the brightness temperature along the jet can be described with a well defined and stable gradient of T_b. Most extragalactic parsec-scale jets which do not show pronounced curvature, show a power-law decrease with increasing distance from the core and power-law indices typically around -2.5 (Kadler 2005). In fact, excluding the E–, F– and H–components from the fit yields a statistically acceptable result ($\chi^2 = 1.3$, 52 d.o.f.) and a gradient of -2.4 ± 0.2. The brightness-temperature gradient of component E is first flat or inverted immediately after the creation of this new component inside 1 mas from the core and turns then over to "normal" values of -2.5 to -2.8 (regime I; compare Fig. 9) through 1997 when the component travels from 1 mas to 2 mas. Between 2 mas and 4 mas, the determination of the brightness-temperature gradient requires an identification of component E with either component E1 or E3 (see below). Independent of the identification, the brightness-temperature gradient eventually changes to very steep values (< -5) outside 5 mas from the core (regime II). Component F begins its very rapid decline in brightness temperature at a very small distance from the core (< 0.7 mas). The T_b-gradient is extremely steep: < -8.

Linear Polarization: From 1995 to 2002, 2 cm-Survey observations were done in left circular polarization only, so that no linear-polarization information can be derived from these data. MOJAVE observations (after 2002) are done in full-polarimetric mode and we have supplemented our 3C 111 VLBA 2 cm data with another full-polarimetric data set

from October 2002 (PI: Taylor). Figure 10 shows our polarization data through September 2005.

In October of 2002, component H is about 2.5 mas from the base of the jet and has a fractional polarization of 5-10% increasing towards the downstream side of the component. The electric vector position angle (EVPA) of the component is approximately aligned with the jet, indicating a transverse magnetic field order as might be expected for a transverse shock propagating down the jet. In this epoch, the jet material just downstream of component H at ~ 3.3 mas from the base of the jet is more highly polarized, exceeding 20% fractional polarization on the jet's southern side, and the EVPA of the polarization turns to be about 45 degrees to the main jet direction.

By August of 2003, component H has entered the region ~ 3.3 mas and its polarization is now similar to the emission in this same region observed in the previous epoch. The fractional polarization of H now climbs sharply to values in excess of 20% toward the jet's southern side while there is no detectable polarization from the northern side of H. The EVPA of H has rotated also to be approximately 45 degrees to the main jet direction; however, the polarization vectors on the southern-most side of H appear to be approximately perpendicular to the local total intensity contours, suggesting an oblique shock or perhaps shearing caused by a differential flow at the southern side of the jet in this location.

After component H passes through this region (epochs April 2004 through September 2005), it breaks into a number of subcomponents as described earlier, and its' polarization gradually becomes more uniform, approaching a consistent level of 5-10% polarization with an EVPA which is approximately perpendicular to the local jet direction indicating magnetic field now ordered along the main jet axis. This is consistent with a differential flow in the jet where one side of the jet flows faster than the other and stretches the magnetic field through shear. Our overall picture then is of an originally transverse shock

interacting with the jet on the southern side of the jet at 3.3 mas from the core. The interaction changes the component's magnetic field through some combination of oblique shock and differential flow resulting in a magnetic field approximately parallel to the jet axis in the later epochs.

It is important to note that the much weaker component, I, develops polarization very similar to H as it passes through this same region, 3.3 mas from the core, with fractional polarization exceeding 20% toward the southern side of the jet with an EVPA at 45 degree angle to the main jet axis. This is also the same region of the jet in which component E broke up into a number of sub-components. In future epochs, we will have the opportunity to follow component K as it passes through this same region.

4. Discussion

In this section, we discuss the 2 cm-Survey and MOJAVE monitoring results for the aftermath of the major outburst in 3C 111 in 1996 and the following component ejections through 2005. We organize the subsections of our discussion according to the downstream distance from the VLBI core where we observe the effect of interest.

4.1. < 1 pc: Forward and Reverse Structures

Numerical simulations (Aloy et al. 2003) show that an abrupt perturbation of the fluid density at the jet injection point during a short time propagates downstream, evolves spreading asymmetrically along the jet and finally splits into two distinct regions. Both of these two regions have enhanced energy density with respect to the underlying jet, and they emit synchrotron radiation. The leading one (the forward shock) has a larger and that the second one has a lower Lorentz factor than the underlying jet. Due to the difference in

bulk Lorentz factors, the above-mentioned two regions should separate with time as they propagate downstream in the jet. The second region is interpreted in the aforementioned simulations by Aloy et al. (2003) as a reverse shock.

Component F matches the description of a backward moving wave associated with the major injection into the jet of 3C 111 after the flux-density outburst of 1996. It follows the trail of component E but at a lower speed. If we identify component F with a reverse shock and component E with the forward shock, it is possible then to compute the size of the shocked region (Perucho et al. 2007). In 1996.82 and 1997.19, E and F are both very bright and separated by only $\sim 0.3\,\mathrm{pc}$ in projected distance. During these two epochs, F is 300 mJy to 500 mJy brighter than the leading component E. Aloy et al. (2003) state that a backward shock can be brighter than a forward shock if the latter is beamed in a cone smaller than the viewing angle due to its larger speed. We have checked the Doppler factors of components E and F for the range of possible viewing angles (see appendix A) and the measured velocities and conclude that this alone cannot explain the brighteness difference between component E and F because the difference in apparent speed is not large enough. Jorstad et al. (2005) point out that backward shocks can be brighter than forward shocks as long as the disturbance is prolonged and there is a continuous entering of particles from the underlying jet through the shock region. Within half a year, between 1997.19 and 1997.66, F looses about half of its brightness. This extraordinarily fast dimming of the backward shock could be because of the lack of input of particles from behind, i.e., a lower plasma ejection rate after the primary injection possibly due to a depletion of the inner accretion disk which feeds the plasma injection.

Component F could also be interpreted as a rarefaction propagating backwards in the reference frame of the ejected blob of gas. A rarefaction is produced in the case that the blob is overpressured with respect to the jet, as this overpressure makes its front to

accelerate in the jet, thus leaving a rarefied region between the head of the blob (forward shock) and its rear part, which is still slower (it moves with the injection velocity). In this case, the emission in component F could be associated to the denser and overpressured gas in the blob which has still not been rarefied. This gas would cease to emit as soon as it reaches the rarefaction, what could also explain the sudden decrease in brightness of this component. An extended discussion on the nature of component F and the evolution of its brightness will be given in Perucho et al. (2007).

4.2. $2-4$ pc: Expansion and Acceleration

It is not *a-priori* clear with which post-split-up component the original feature E should be identified after 1999. A natural identification would be the leading component E1 but requires an acceleration of this component (see Fig. 4) from $\beta_{app,E} = 3.26 \pm 0.07\,c$ to $\beta_{app,E1} = 5.5 \pm 0.1\,c$ between 1998.18 and 1999.39. This can be interpreted in terms of an expansion of the jet in a rarefied medium. Taking an angle to the line of sight of 19° (see appendix A), the component would be accelerated from $\beta = 0.956$ ($\gamma \sim 3.4$)to $\beta = 0.995$ ($\gamma \sim 10.3$). The increase of velocity decreases for smaller viewing angles. Identifying component H with component H1 also implies an acceleration of the former at about the same distance to the source, although, in this case, the flux density decay of component H1 with respect to the trailing components H2, H3 and H4 remains to be understood. Thus, we could conclude that components enter a region with lower density or a steeper density gradient between 2 and 4 mas from the source.

Direct identification of component E with component E1 is not straightforward in the frame of expansion, as component E1 in epoch 1999.39 is smaller than component E in 1998.18 (see Table 2). However, component E3 in epoch 1999.39 is larger than component E in 1998.18. We can interpret this as component E including components E1 and E3

(and maybe E4). These components would be indistinguishable to our instruments before 1999.39. In fact, Jorstad et al. (2005) monitored 3C 111 between 1998 and 2001 with the VLBA at 43GHz. They find an emission complex, that can be identified with our component E, that gradually stretches out as it travels from ~ 2 mas from the core in 1998 to $\sim 5-8$ mas from the core in 2001. Their leading component C1 can be identified with our component E1, their component c2 with E2 and their c1 with E3. At their higher angular resolution, Jorstad et al. (2005) can separate components C 1 and c 1 already in early 1998. In agreement with our analysis at 15 GHz, Jorstad et al. (2005) detect c2 (E2) about a year after they detect c1 (E3). They don't detect a component corresponding to E4 but this may be an effect of partially resolving out the jet structure at their higher observing frequency, particularly in later epochs. It is further interesting to note that the speeds seem to match at both frequencies: E1 (C1) has 1.69 ± 0.04 mas/yr at 15 GHz and 1.77 ± 0.06 mas/yr at 43 GHz, E2(c2) has 1.29 ± 0.06 mas/yr at 15 GHz and 1.23 ± 0.04 mas/yr at 43 GHz and E3(c1) has 1.22 ± 0.05 mas/yr at 15 GHz and 1.07 ± 0.02 mas/yr at 43 GHz. The discrepancy in the speed of E3 and c1 seems to be due to a slight acceleration of E3 after 2002. A fit to the 15 GHz data of E3 between 1999 and 2002 alone yields a slower speed of ~ 1.0 mas/yr similar to the speed of c1 in the same time period at 43GHz. In their work, they don't report acceleration of components from 2 to 4 mas. However, this is likely due to the fact that their observations started in early 1998, thus missing the first observations of component E presented in this paper, when its speed has been measured to be smaller.

4.3. $2-6$ pc: Recollimation of the Jet

Inspection of Fig. 9 shows that the back-extrapolation of the brightness temperature to the region of component E yields at least two orders of magnitude too high values if this

extrapolation is based on the gradient given by E1. The too-low brightness temperature of component E cannot be explained by opacity effects because the radio-light curve in Fig. 1 shows that the source was again in an optically thin state from 1997 on. Moreover, if we identify component E with E1, it is Doppler deboosted from epoch 1998.18 to 1999.39 due to the acceleration in a relatively large viewing angle, and thus we are not able to explain the increase in brightness temperature in terms of Doppler boosting. However, compact sub-components may have larger brightness temperatures, so that the T_b values plotted in Fig 9 for E inward of ~ 3 mas may represent lower limits for compact components already embedded in the unresolved structure.

Not only E/E1 but also components G and H show an increase in total flux density several milliarcseconds downstream. Compared to E/E1, these somewhat weaker components exhibit their flux-density maxima at somewhat larger distances from the core (compare Fig. 6 and Fig. 7). This can be explained if the components travel through a mild standing shock in a recollimation region. The material in the components is expected to be overpressured with respect to its environment, thus expanding into it. After the initial expansion, the components become underpressured with respect to the underlying flow. The resulting recollimation leads to the formation of a shock, whose strength depends on the initial degree of overpressure of the material in the component. This process explains the increase in flux density and brightness temperature as due to compression of the gas in the recollimation. In Figs. 6 and 7, we see that the flux density of component E increases closer to the core than for component G and H, which is consistent with the former being more overpressured than the latter, expanding faster and recollimating earlier. It also explains why we see a significant acceleration only in the faster expanding, brighter component E/E1.

Finally, after this mild recollimation, the fluid becomes overpressured with respect to

its environment, thus further expanding and accelerating downstream.

4.4. An Alternative Scenario: Elastic Deflection between 2 and 4 pc

The acceleration of component E can also be interpreted on the basis of an elastic-deflection event that would produce an apparent acceleration of the component due to the jet approaching the observer's line of sight. However, a large change in the angle to the line of sight is implied: from $\sim 24°$ to $\sim 11°$ (Kadler 2005). In lack of a pronounced change in the component position angle, i.e., the observed angle projected onto the the plane of the sky, this deflection would have to happen almost perpendicular to the projection plane clearly disfavoring this scenario. The elastic-deflection model, however, is capable of explaining the "bump" in the brightness-temperature gradient between 3 and 5 mas (compare Fig. 7) via differential Doppler boosting associated with the change in the angle to the line of sight. A de-projection according to the elastic-deflection model results to a smooth brightness-temperature gradient ~ -3.75 (Kadler 2005).

4.5. ~ 3 pc: Magnetic Field Shearing or Faraday-Screen Inhomogenities

The polarization behavior of components H and I can be understood in terms of an interaction between the jet and the external medium at a distance of 3.3 mas in the jet. It should be noted that no strong shock is needed at this location in the jet in order to explain the polarization characteristics. A re-ordering of the magnetic field, e.g., via shearing at a contact surface with the ambient medium would be sufficient. The observed north-south gradient in linear polarization suggests that such a contact surface persists at the southern boundary of the jet beam at a distance of 3.3 mas downstream the jet core. This region may be identified with the recollimation region (see Sect. 4.3 at about the same position

in the jet. In this picture, the jet-medium interaction may form an effective nozzle which accelerates the jet on one edge relative to the other.

An alternative explanation for the observed polarization structure and dynamics of 3C 111 can be found by considering an inhomogeneous external Faraday screen. Such a screen could produce the observed differential rotation of the EVPA while a component travels through a given region along the jet. Zavala & Taylor (2002) observed 3C 111 with the VLBA and produced a Faraday rotation-measure map between 8 GHz and 15 GHz. They find strong Faraday rotation ($\sim 730\,\mathrm{rad\,m^{-2}}$) at right the same distance from the core (3.3 mas) where we see the swing of the EVPA of the component H and steeply decreasing Faraday rotation further downstream. Note that $730\,\mathrm{rad\,m^{-2}}$ translate to 17 degrees of rotation at 15 GHz which alone is not enough to explain the change in EVPA that we observe while component H travels through this region. On the other hand, the steep decrease of the Faraday rotation measure up- and downstream of this region is again in agreement with a change of the external gas density at this point, which in turn may be identified with the pressure gradient responsible for the component expansion and accelleration.

4.6. $3-5$ pc: Formation of Trailing Components

The components E2, E3, and E4 can be interpreted as trailing components forming in the wake of the leading E1 which is identical with the original component E. This scenario is attractive because the basic concept of trailing components as introduced by Agudo et al. (2001) predicts the formation of trailing features in the wake of the initial perturbation in the jet flow. Such a behaviour has been found associated with bright superluminal jet components in Centaurus A and 3C 120 (Tingay et al. 2001; Gómez et al. 2001).

The interaction of the external medium with a strong shock pinches the surface of the jet, leading to the production of pinch body mode Kelvin- Helmholtz instabilities: the trailing features. Hence, a single strong superluminal shock ejection from the jet nozzle may lead to the production of a multiple set of emission features through this mechanism. The trailing features have a characteristic set of properties, which make them recognizable with high resolution VLBI: they form in the wake of strong components instead of being ejected from the core of VLBI jets, they are related to oblique shocks, they are always slower than the leading feature, and (if the underlying jet has a certain opening angle) they should be generated with a wide range of apparent speeds (from almost stationary near the core to superluminal further downstream). Moreover, Agudo et al. (2001) showed that the separation between the trailing components increased downstream due to their motion down a pressure gradient.

All this is in agreement with what we observe in the trailing components of E 1 and with our interpretation of an expansion of the jet in a density decreasing ambient medium. For the time range covered by their observations (1998.23 to 2001.28), Jorstad et al. (2005) also identified the trailing phenomenology in this source

The north-south gradients detected in the linear-polarization mission in the region where the trailing features are formed, indicates an oblique shock structure. The steep brightness-temperature gradients of the trailing components indicate that the particle and magnetic field density associated with these components evolve in a different way compared to the "normal" jet flow. These shocked regions may be stronger overpressured with respect to their environment, making them to expand faster. This fast expansion implies a larger positive value of l, which, however, is compensated by an even larger (negative) value of n and $b(1-\alpha)$ in equation 3.

Pinching modes of the Kelvin-Helmholtz instability were shown to couple to the trailing

components observed in the simulations in Agudo et al. (2001). In the case of components E2-E4, the distance between them ranges from 0.7-0.8 mas at the first epochs in which they are observed, to almost 2.0 mas in the latest epochs. Taking into account that: a) their FWHM is of the same order (see Table 2); b) that these wavelengths have to be corrected for the geometrical and relativistic effects, which turns out in a maximum intrinsic wavelength of ~ 0.7 mas, and c) that the size of the components can be of the order or smaller than the jet radius (Perucho & Lobanov 2007), this implies coupling of the pinching to wavelengths of the order or smaller than the jet radius. Perucho et al. (2007) have shown that resonant Kelvin-Helmholtz instabilities associated to high order body modes appear in sheared jets at these wavelengths. These modes have larger growth rates than low order body modes or surface modes, and their growth brings the jet to a final quasi-steady state in which it remains well collimated and generates a hot shear-layer which shields the core of the jet from the ambient medium. Interestingly, the jet in 3C 111 is known to be well collimated up to kiloparsec scales. Further research in this direction is needed in order to check the influence of the resonant modes in the long term evolution of this jet.

A by-product of the interpretation of these components as Kelvin-Helmholtz instabilities is the fact that it allows us to put constraints to the velocity of the jet. We can regard the wave speed as the minimum speed of the jet flow, as KH modes have an upper limit in their wave speeds that is precisely the velocity of the flow in which they propagate. The upper limit is given by the speed of E1, interpreted as a shock wave, that has to be thus faster than the underlying flow. In this picture, we would have the structure E1 moving with Lorentz factor $\gamma \sim 8.3$ through a jet with Lorentz factor $8.3 > \gamma_j \geq 4.6$ in the accelerated region (post 1999.39), where the lower limit is given by the Lorentz factor of component E2, the fastest of the three trailing components identified here.

5. Summary and Conclusions

In this paper, we have performed a scrutiny of the parsec-scale jet kinematics and the interaction of the jet with its ambient medium in the broad-line radio galaxy 3C 111. Our analysis has demonstrated that a variety of processes influence the jet dynamics in this source: a plasma injection into the jet beam associated with a major flux-density outburst leads to the formation of multiple shocks that travel at different speeds downstream and interact with each other and with the ambient medium. The primary perturbation causes the formation of a forward and a backward shock (or rarefaction). The latter fades away so fast that is likely to remain undetected in minor ejections. A separate work by Perucho et al. (2007) focuses on the nature and characteristics of these initial components. Several parsecs downstream, the jet plasma enters a region of rapidly decreasing external pressure, expands into the jet ambient medium and accelerates. In the following, the plasma gets recollimated and trailing features are formed in the wake of the leading component.

A particularly interesting aspect of the source 3C 111 in the light of this and other recent works is that it is one of the very rare non-blazar gamma-ray bright AGN. Besides Centaurus A (Sreekumar et al. 1999) and the possible identification of NGC 6251 with the EGRET source 3EG J1621+8203 (Mukherjee et al. 2002), 3C 111 is the only AGN whose jet-system is inclined at a relatively large angle to the line of sight and that has a reliable EGRET identification: After a careful multiwavelength catalog study, (Sguera et al. 2005) gave new rise to the possible identification of the EGRET source 3EG J0416+3650 with 3C 111, which was first considered by Hartman et al. (1999) but not generally accepted because of the large positional offset. Very recently, Hartman & Kadler (2007) found that 3EG J0416+3650 is actually composed out of two distinct components of which one is in excellent positional agreement with the location of 3C 111. Compared to blazars, the large inclination angle and the relatively small distance of 3C 111 allow us to resolve structures

along the jet that are as small as parsecs in deprojection and which would be heavily blended with adjacent features in blazar jets. As demonstrated in this paper, VLBI observations of 3C 111 probe a variety of physically different regions in a relativistic extragalactic jet such as a compact core, superluminal jet components, recollimation shocks and regions of interaction between the jet and its surrounding medium, which are all possible sites of gamma-ray production. This makes 3C 111 –if it will be detected by GLAST– a key source in the quest for an understanding of the origin of gamma-rays from extragalactic jets.

We can conclude that our observations of 3C 111 are qualitatively in remarkable agreement with numerical relativistic magnetohydrodynamic structural and emission simulations of jets such as the ones presented by Agudo et al. (2001) and Aloy et al. (2003). Future VLBI observations of 3C 111 may be capable of putting hard quantitative constraints on the parameters of jet simulations Observations at multiple radio frequencies may allow the effects of jet-intrinsic magnetic-field variations and external Faraday-screen inhomogenities or temporal variations to be disentangled. Future gamma-ray observations may find 3C 111 to be a primary target for the spatial location of gamma-ray production sites and the combination with VLBI data and spectral data at intermediate wavelengths (optical, IR, X-ray) may allow a better determination of jet parameters and relativistic beaming effects than in most blazars. As a prerequisite, it is essential to obtain full-polarimetric multi-frequency VLBI observations, densely sampled in time. Such data at 15 GHz are on the way as part of the next phase of the MOJAVE program, in which 3C 111 is being observed every two months.

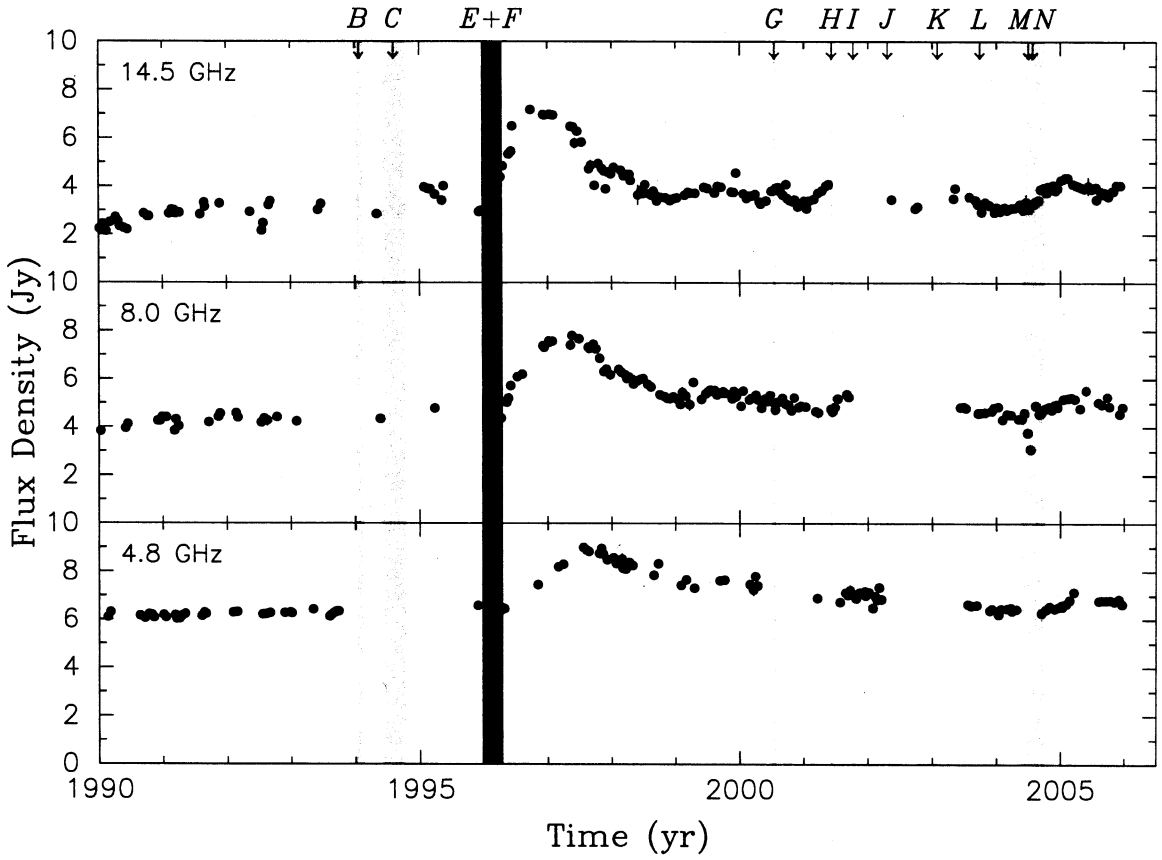

Fig. 1.— Radio-light curves of 3C 111 at 4.8 GHz, 8 GHz, and 14.5 GHz from the UMRAO monitoring program. The shaded areas indicate the ejection epochs of the individually labeled jet components. The lightest shading corresponds to minor ejections of the relatively weak components I,J,K,L with flux densities S below 0.2 Jy, medium shading corresponds to components B,C,G,H,M,N with 0.2Jy $< S <$ 0.6Jy and the darkest shading to components E and F with $S >$ 0.6Jy.

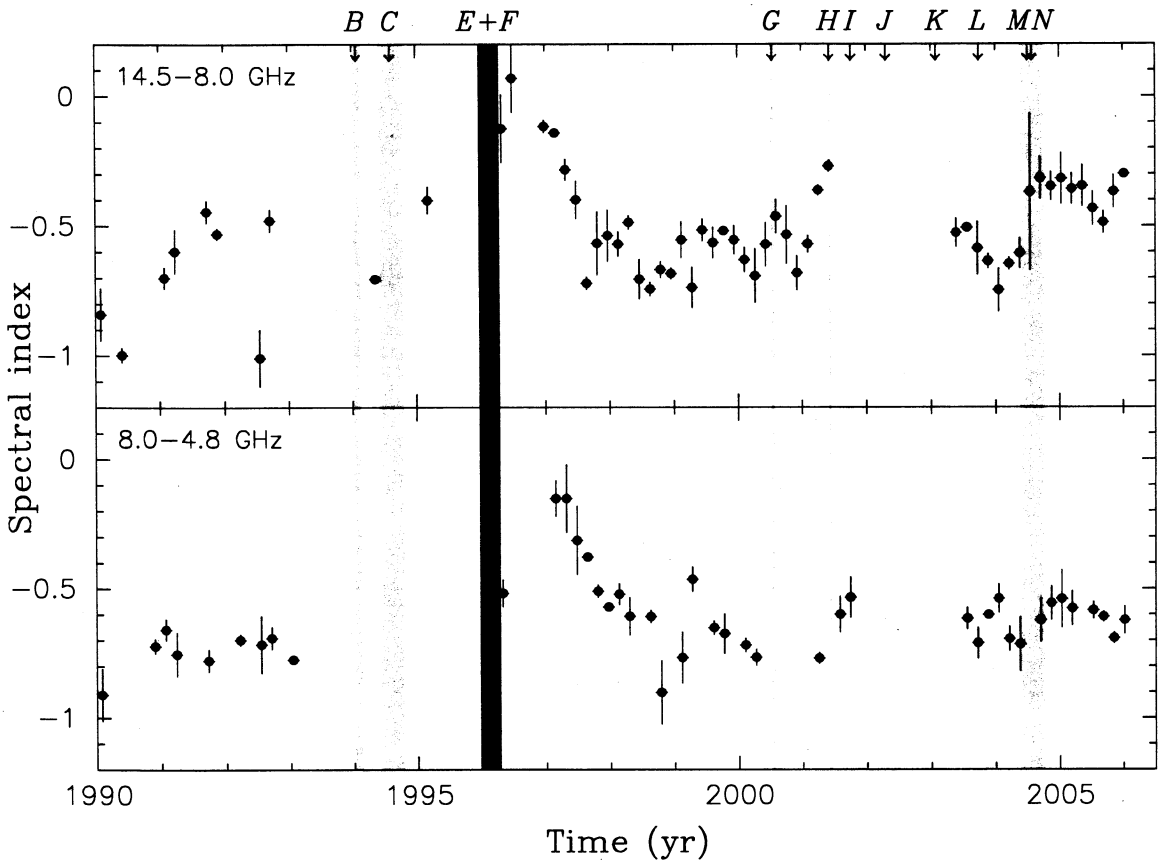

Fig. 2.— Spectral-index curves of 3C 111 between 14.5 GHz and 8 GHz (top), and 8 GHz and 4.8 GHz (bottom) from the UMRAO monitoring program. The shaded areas are the same as in Fig. 1.

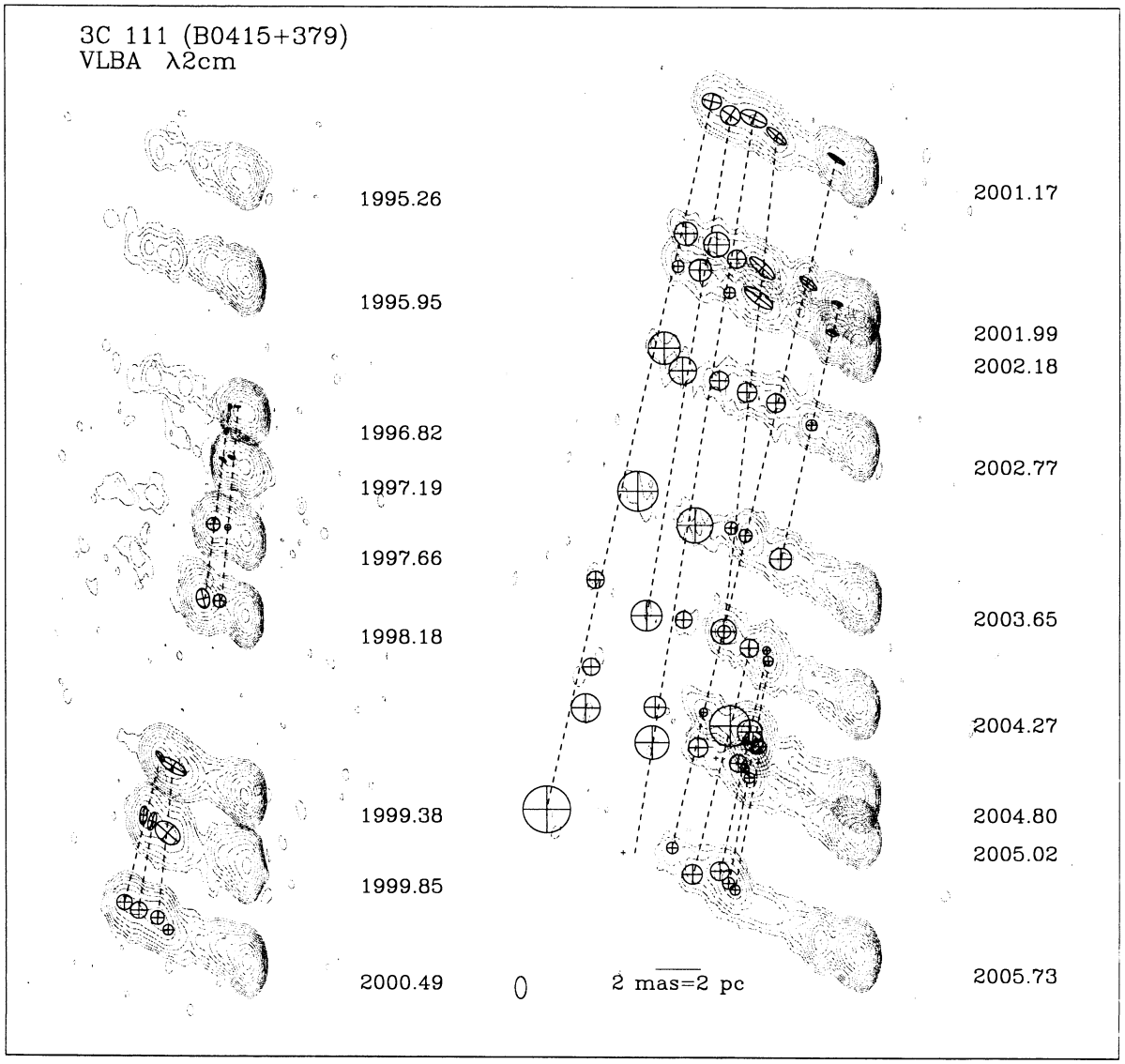

Fig. 3.— Naturally weighted images of the parsec-scale jet of 3C 111 from the 2 cm VLBA monitoring. A common restoring beam of (0.5 × 1.0) mas at P.A. 0° was used. The total recovered flux density in each image, the rms, and the lowest contours in this image are given in Table 1. Contours increase logarithmically. Only components E, G, H and their corresponding trailing components are indicated.

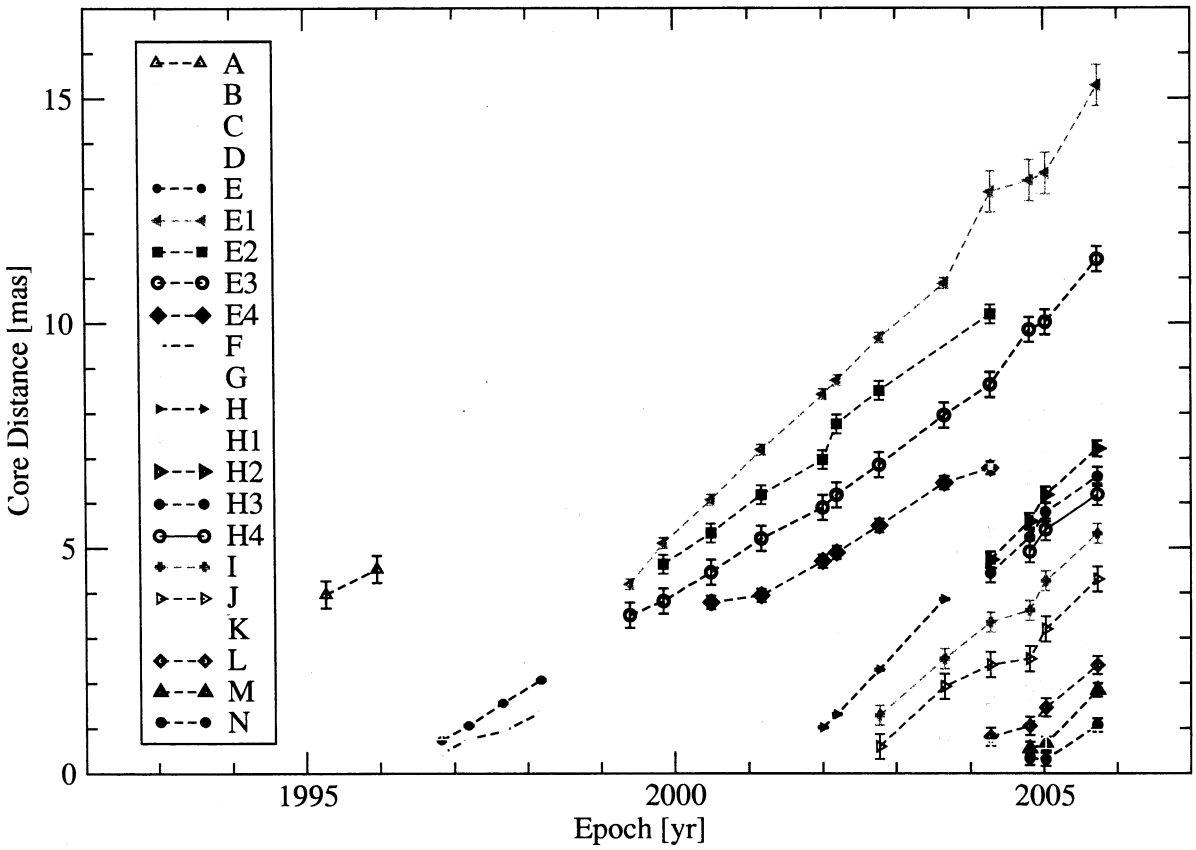

Fig. 4.— Core separation of model-fit components vs. time. Crosses represent components which could not be cross identified over the epochs.

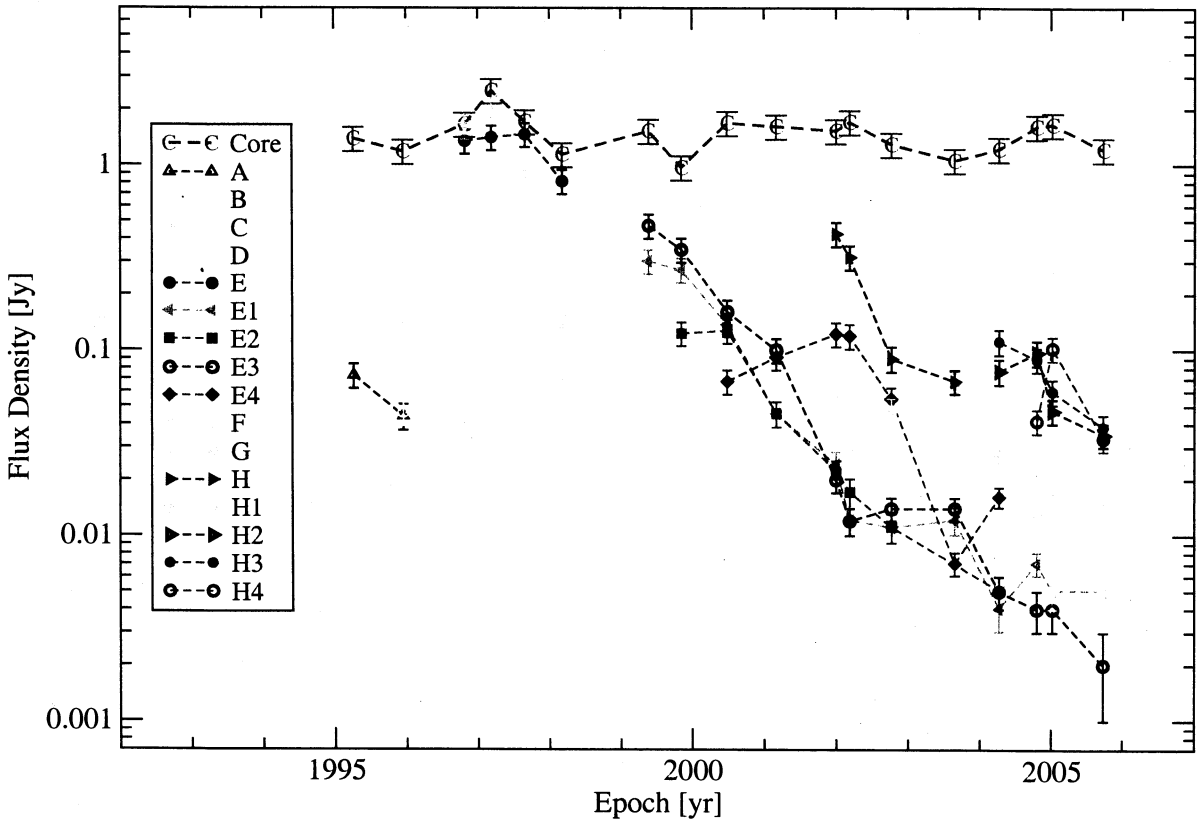

Fig. 5.— Flux-density evolution of the core and the jet components with time. For clarity, only components ejected before 2001.50 are shown. Note that components E4 and G are blending in epoch 2004.27 and that the flux density of E4 may be overestimated for this epoch.

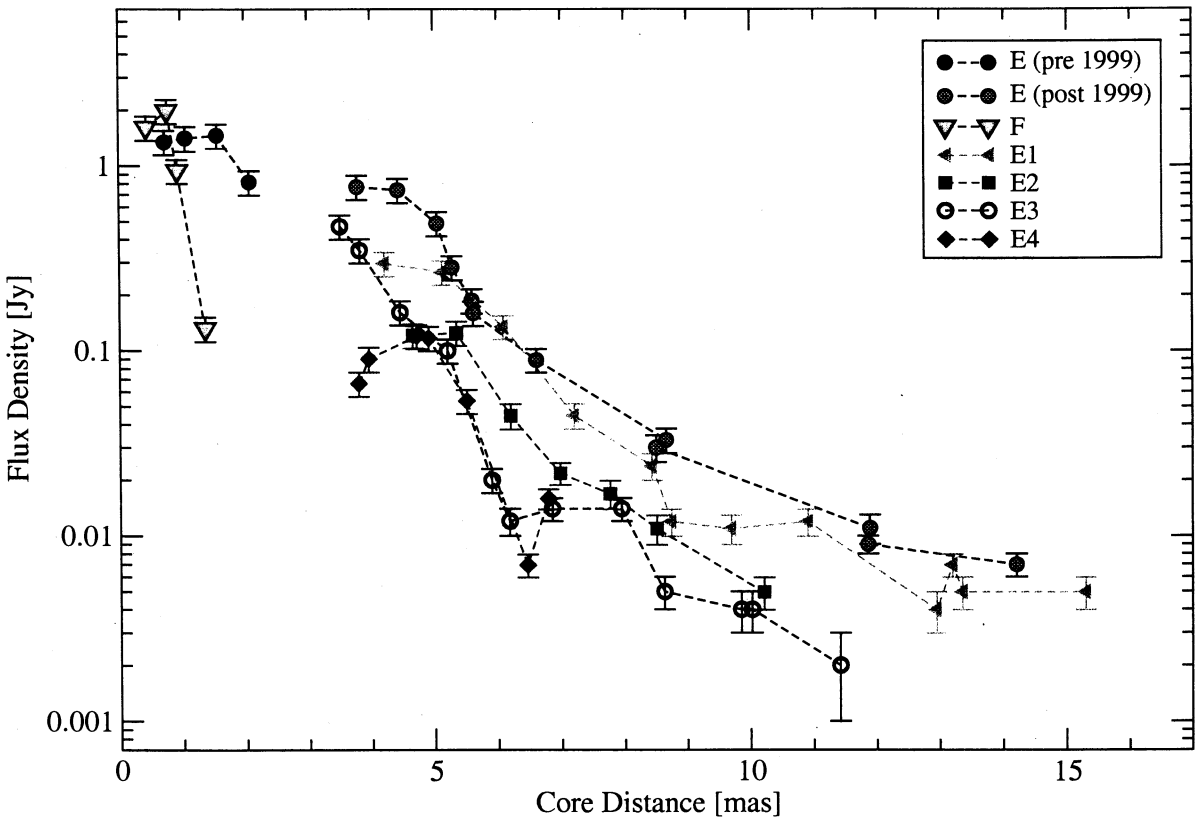

Fig. 6.— Flux-density evolution of component E and its trailing components with traveled distance from the core. Note that component E 4 is blending with component G in epoch 2004.27 and that its flux density may be overestimated for this epoch.

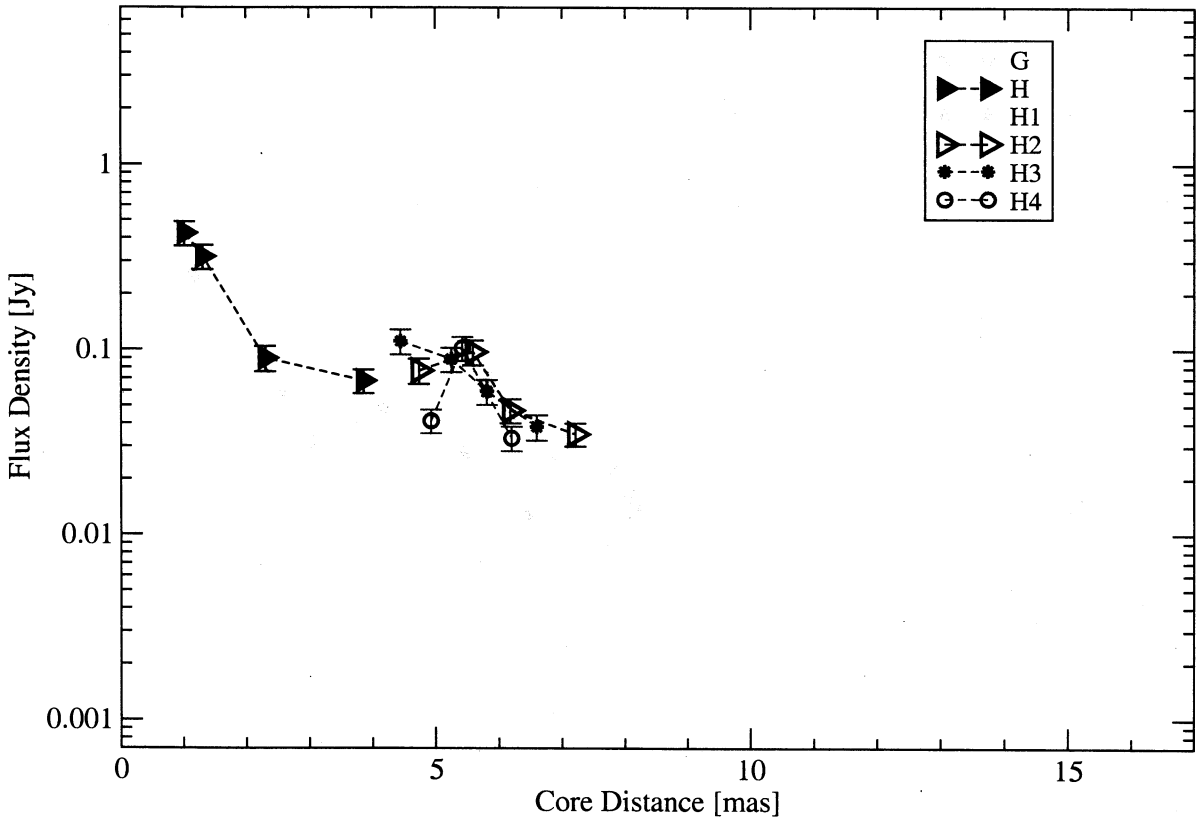

Fig. 7.— Flux-density evolution of component G and H and its trailing components with traveled distance from the core.

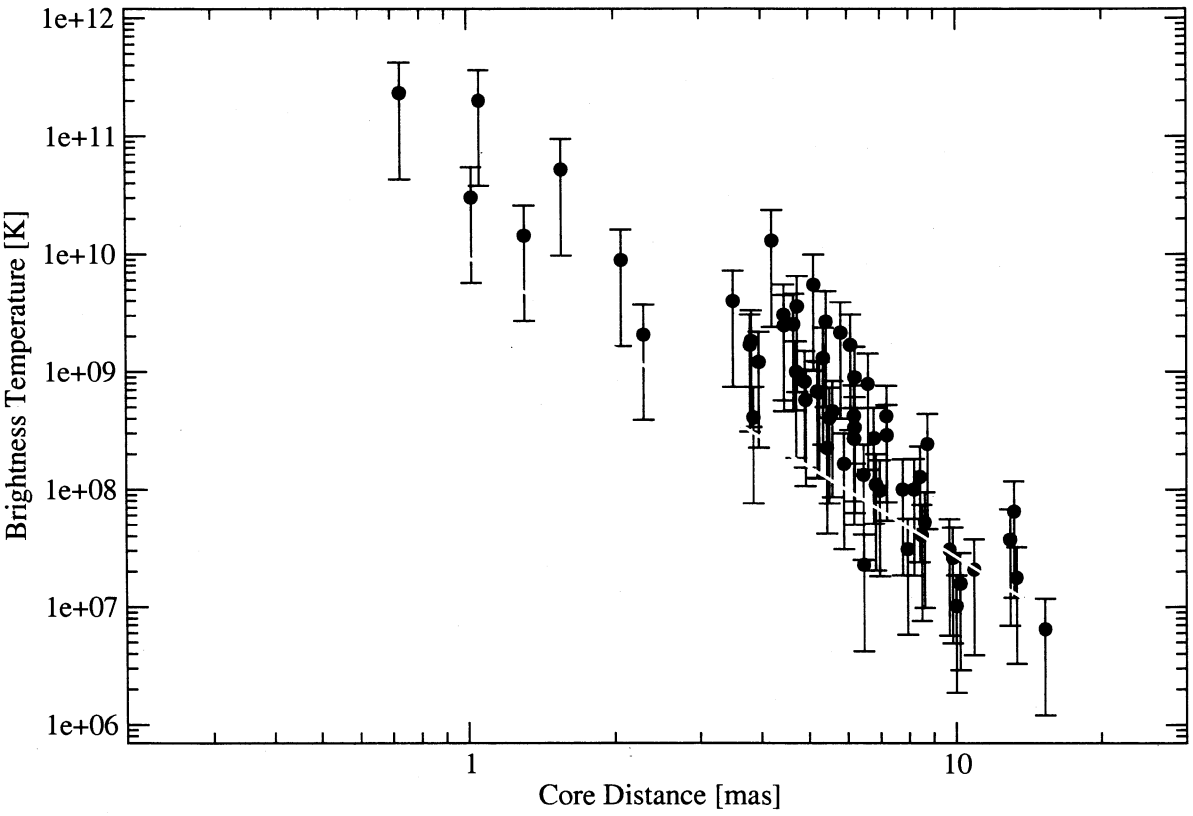

Fig. 8.— Brightness temperatures of model-fit components as a function of their distance to the core. The brightness temperatures of components belonging to the E–, F– and H–components are indicated by filled black circles. The solid line represents a least-squares fit to all but the E–, F– and H–components (slope of regression curve: -2.4 ± 0.2).

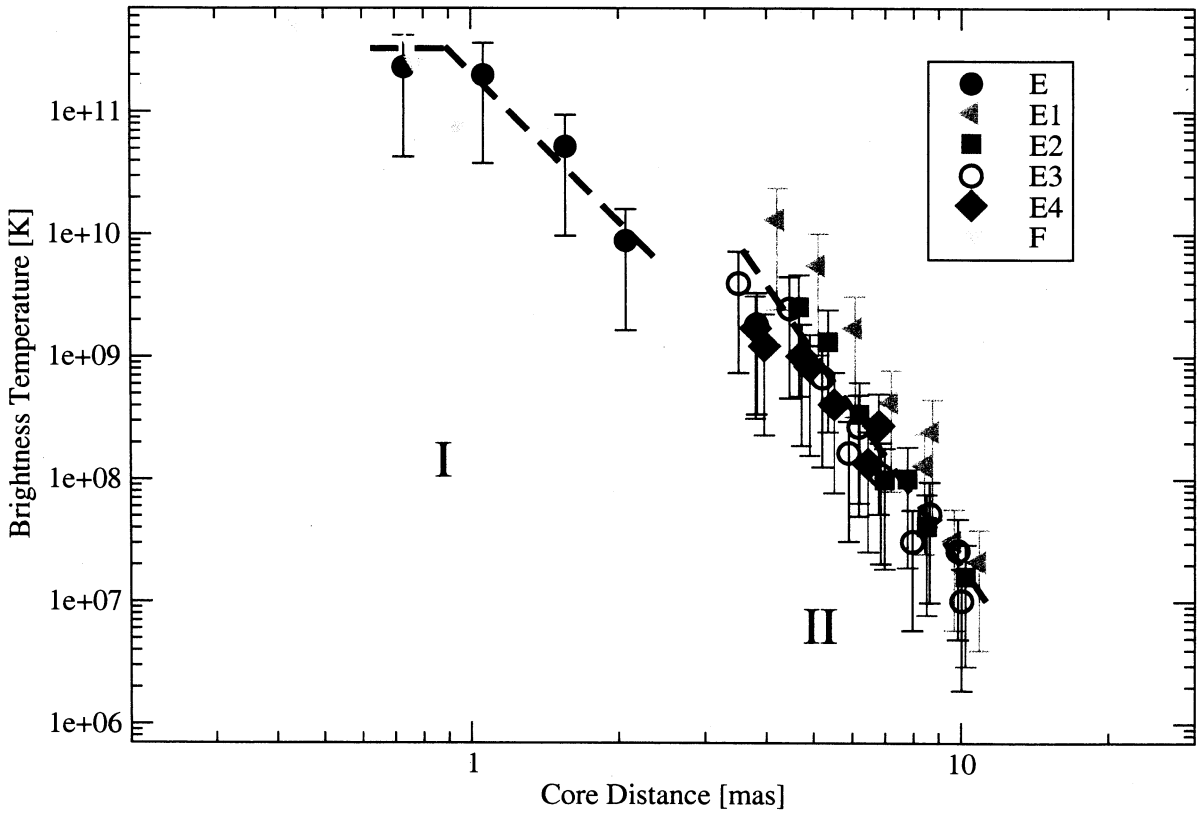

Fig. 9.— Brightness temperatures of component and its leading and trailing components as a function of their distance to the core. The three regimes of brightness-temperature gradient discussed in the text are indicated with dashed lines.

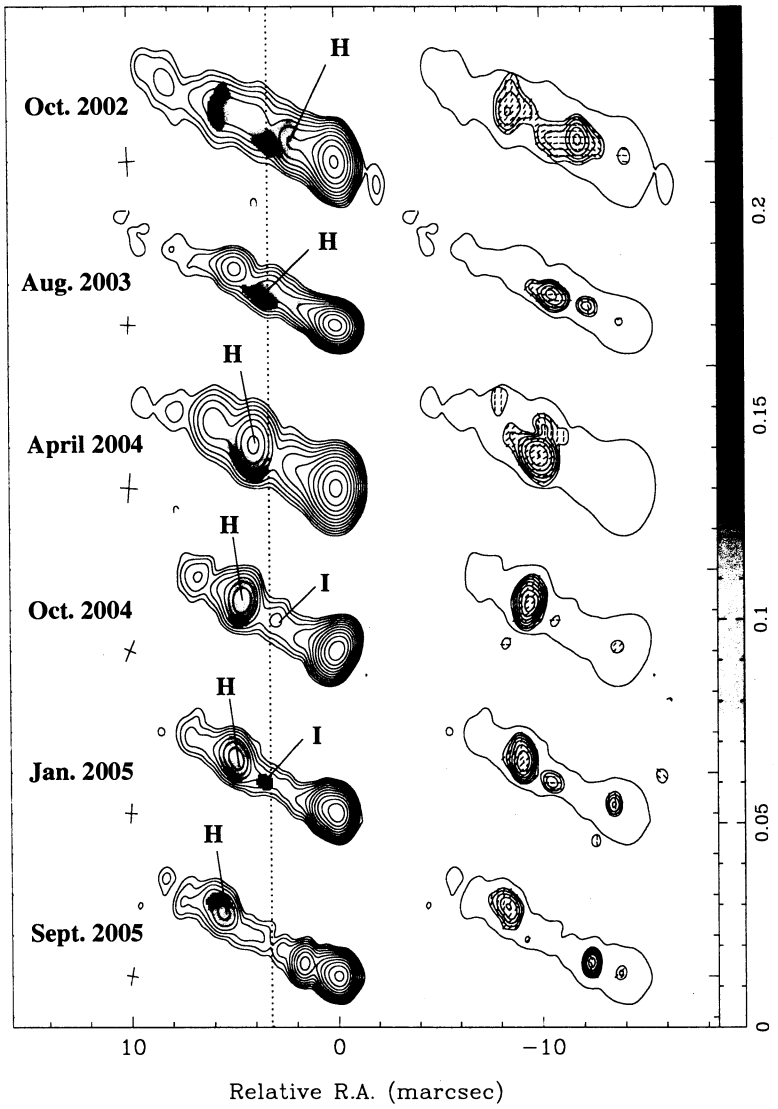

Fig. 10.— Naturally weighted images of the linear-polarization structure of 3C 111 between 2002 and 2005. The restoring-beam dimensions and orientations for each epoch are indicated by a cross figure to the left of each Stokes-I image. Stokes I contours start a 1 mJy/beam and increase in steps of $\times 2$. Fractional polarization is over-plotted on the Stokes-I contours in color. To the right of the Stokes-I images are the polarization intensity contours starting at 1 mJy/beam and increasing in steps of $\times\sqrt{2}$. The polarization contours are over-plotted with tick-marks representing the electric vector position angle. A single Stokes-I contour surrounds the polarization image to show registration.

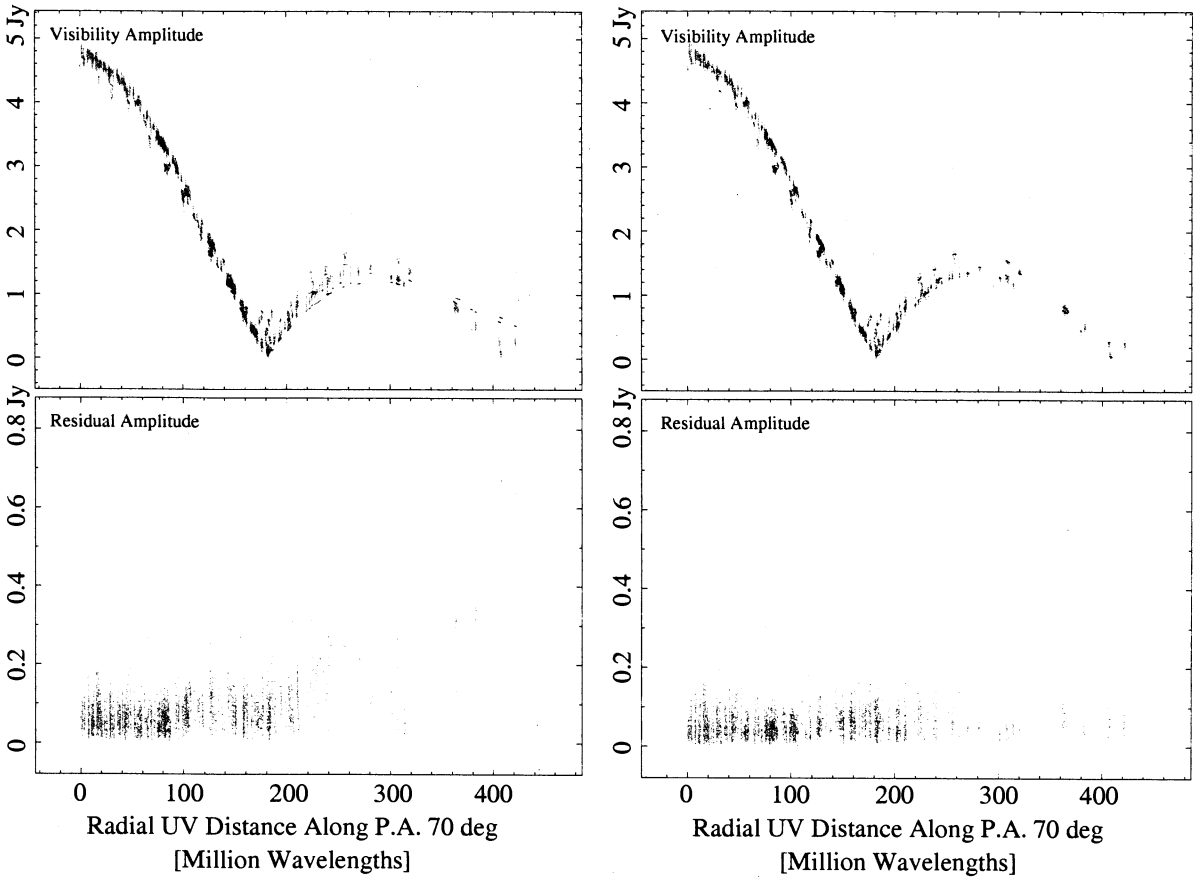

Fig. 11.— Visibility amplitudes projected radially along P.A. 70° for the 1996.82 observation of 3C 111. The double-peak indicates the presence of a bright structure within less than a milliarcsecond of the core. The top left panel shows a model fitted to the data consisting of one model component for the newly ejected jet feature and the residuals of this model are shown in the bottom left panel. Up to $\sim$ 600 mJy of correlated flux remain unmodeled. The right panels show the same data fitted by a model consisting of two components (corresponding to E and F).

Table 1: Journal of VLBA 2cm Survey observations of 3C 111 analyzed in this study.

Epoch	Code	$S_{\rm tot}$ [Jy]	rms [mJy/beam]	$C^{\rm a}$ [mJy/beam]
1995.27	BK 016	2.6	1.8	5.6
1995.96	BK 037A	1.8	1.1	1.6
1996.82	BK 37D	4.8	0.5	2.4
1997.19	BK 048	6.0	1.3	12.3
1997.66	BK 052A	4.1	1.6	3.5
1998.18	BK 052B	2.0	2.1	1.5
1999.39	BK 068A	2.6	0.6	1.5
1999.85	BK 068C	2.4	1.3	2.5
2000.49	BT 051	2.6	0.2	1.0
2001.17	BK 068E	2.1	0.4	1.0
2002.00	BR 077D	2.2	0.4	1.4
2002.19	BR 077I	2.2	0.3	1.1
2002.77	BL 111C	1.6	0.2	1.5
2003.65	BL 111J	2.1	0.2	1.1
2004.27	BL 111L	1.9	0.2	1.4
2004.80	BL 111P	2.7	0.2	0.9
2005.02	BL 123A	3.0	0.1	1.7
2005.73	BL 123O	2.4	0.1	0.7

[a] Lowest contour in Fig. 3

Table 2. Model fit parameters

ID	Flux Density [mJy]	Radius [mas]	P.A.[a] [°]	FWHM [mas]	ratio	ϕ[°]
			1995.27			
0	1371.04 ± 205.66	0.00	24.00	0.33 ± 0.60	0.43	56.22
D	876.06 ± 131.41	0.61 ± 0.30	61.18	0.21 ± 0.54	1.00	–
C	149.59 ± 22.44	1.14 ± 0.21	60.80	0.41 ± 0.64	1.00	–
B	112.85 ± 16.93	2.06 ± 0.29	69.41	0.62 ± 0.79	1.00	–
A	73.30 ± 10.99	3.97 ± 0.30	70.69	0.00 ± 0.50	1.00	–
			1995.96			
0	1173.64 ± 176.05	0.00	–	0.35 ± 0.12	0.59	47.42
D	353.66 ± 53.05	0.73 ± 0.30	61.85	0.30 ± 0.12	1[b]	–
C	145.60 ± 21.84	1.72 ± 0.21	62.73	0.38 ± 0.13	1[b]	–
B	46.15 ± 6.92	3.37 ± 0.29	70.25	0.61 ± 0.16	1[b]	–
A	43.54 ± 6.53	4.53 ± 0.30	69.99	0[d]	1[b]	–
			1996.82			
0	1645.03 ± 246.75	0.00	–	0.26 ± 0.11	0.17	60.63
F	1608.94 ± 241.34	0.44 ± 0.07	54.71	0.31 ± 0.12	0.19	87.46
E	1344.91 ± 201.74	0.73 ± 0.02	67.83	0.23 ± 0.11	0.61	35.24
X1	121.29 ± 18.19	1.06 ± 0.3	61.59	0.33 ± 0.12	1[b]	–
C	38.24 ± 5.74	3.28 ± 0.21	66.12	0.88 ± 0.20	1[b]	–
B	38.04 ± 5.71	4.76 ± 0.06	68.08	0.66 ± 0.16	1[b]	–
			1997.19			
0	2490.20 ± 373.53	0.00	–	0.38 ± 0.13	0.26	62.36

Table 2—Continued

ID	Flux Density [mJy]	Radius [mas]	P.A.[a] [°]	FWHM [mas]	ratio	ϕ[°]
F	1980.30 ± 297.05	0.77 ± 0.07	-55.51	0.34 ± 0.12	0.39	57.52
E	1410.05 ± 211.51	1.06 ± 0.02	71.09	0.34 ± 0.12	0.35	51.00
C	32.15 ± 4.82	3.72 ± 0.21	65.48	0.23 ± 0.11	1[b]	–
B	35.26 ± 5.29	5.45 ± 0.06	67.95	0.72 ± 0.18	1[b]	–
			1997.66			
0	1697.09 ± 254.56	0.00	–	0.51 ± 0.14	0[c]	59.71
F	940.20 ± 141.03	0.93 ± 0.07	60.22	0.27 ± 0.11	1[b]	–
E	1461.49 ± 219.22	1.56 ± 0.02	67.18	0.40 ± 0.13	1[b]	–
			1998.18			
0	1128.63 ± 169.29	0.00	–	0.82 ± 0.19	0.47	6.27
F	131.71 ± 19.76	1.36 ± 0.07	59.83	0.59 ± 0.16	1[b]	–
E	815.70 ± 122.35	2.07 ± 0.02	67.53	0.90 ± 0.21	0.65	11.93
			1999.39			
0	1509.63 ± 226.44	0.00	–	0.38 ± 0.13	0[c]	64.00
X3	225.98 ± 33.90	0.59 ± 0.30	62.46	0.14 ± 0.10	1[b]	–
X2	54.38 ± 8.16	1.25 ± 0.30	65.08	0.56 ± 0.15	1[b]	–
E3	470.42 ± 70.56	3.51 ± 0.28	68.80	1.34 ± 0.29	0.37	57.41
E1	298.52 ± 44.78	4.21 ± 0.12	66.02	0.56 ± 0.15	0.42	35.72
			1999.85			
0	960.22 ± 144.03	0.00	–	0.78 ± 0.19	0.41	-4.69
X4	743.68 ± 111.55	0.55 ± 0.30	59.07	1.13 ± 0.25	0.58	61.59

Table 2—Continued

ID	Flux Density [mJy]	Radius [mas]	P.A.[a] [°]	FWHM [mas]	ratio	ϕ[°]
E3	349.03 ± 52.35	3.82 ± 0.28	67.78	1.26 ± 0.27	0.69	50.04
E2	122.27 ± 18.34	4.66 ± 0.21	65.12	0.84 ± 0.20	0.39	-16.32
E1	267.68 ± 40.15	5.12 ± 0.12	64.17	0.84 ± 0.19	0.40	-7.05
			2000.49			
0	1668.98 ± 250.35	0.00	–	0.33 ± 0.12	0.11	66.21
X7	249.65 ± 37.45	0.65 ± 0.30	56.02	0.45 ± 0.13	1[b]	–
X6	133.82 ± 20.07	1.31 ± 0.30	59.94	0.48 ± 0.14	1[b]	–
X5	43.07 ± 6.46	2.34 ± 0.30	66.11	0.71 ± 0.17	1[b]	–
E4	66.54 ± 9.98	3.80 ± 0.15	68.04	0.47 ± 0.14	1[b]	–
E3	160.55 ± 24.08	4.46 ± 0.28	63.86	0.61 ± 0.16	1[b]	–
E2	125.58 ± 18.84	5.35 ± 0.21	64.62	0.74 ± 0.18	1[b]	–
E1	135.77 ± 20.37	6.08 ± 0.12	64.13	0.68 ± 0.17	1[b]	–
			2001.17			
0	1596.68 ± 239.50	0.00	–	0.44 ± 0.13	0[c]	61.41
G	243.56 ± 36.53	1.13 ± 0.07	58.96	0.88 ± 0.20	0.22	54.85
E4	91.23 ± 13.68	3.96 ± 0.15	66.28	1.11 ± 0.24	0.35	48.34
E3	99.76 ± 14.96	5.21 ± 0.28	62.80	1.24 ± 0.27	0.54	65.22
E2	45.34 ± 6.80	6.20 ± 0.21	66.06	0.91 ± 0.21	0.92	55.42
E1	45.18 ± 6.78	7.20 ± 0.12	64.16	0.86 ± 0.20	0.83	75.97
			2002.00			
0	1514.03 ± 227.10	0.00	–	0.49 ± 0.14	0.09	61.18

Table 2—Continued

ID	Flux Density [mJy]	Radius [mas]	P.A.[a] [°]	FWHM [mas]	ratio	ϕ[°]
H	424.80 ± 63.72	1.02 ± 0.02	64.67	0.46 ± 0.14	0.39	66.86
G	60.57 ± 9.09	2.59 ± 0.07	58.88	0.94 ± 0.21	0.33	50.61
E4	121.10 ± 18.16	4.72 ± 0.15	64.66	1.40 ± 0.30	0.35	47.76
E3	19.67 ± 2.95	5.90 ± 0.28	65.92	0.82 ± 0.19	1[b]	–
E2	21.62 ± 3.24	6.98 ± 0.21	64.03	1.12 ± 0.25	1[b]	–
E1	24.46 ± 3.67	8.43 ± 0.12	65.14	1.04 ± 0.23	1[b]	–
			2002.19			
0	1688.54 ± 253.28	0.00	–	0.56 ± 0.15	0.09	63.02
H	317.77 ± 47.66	1.31 ± 0.02	64.52	0.48 ± 0.14	0.56	65.20
G	29.58 ± 4.44	3.07 ± 0.07	57.88	0[c]	1[b]	–
E4	118.14 ± 17.72	4.91 ± 0.15	64.22	1.51 ± 0.32	0.36	52.47
E3	12.28 ± 1.84	6.18 ± 0.28	67.59	0.51 ± 0.14	1[b]	–
E2	17.46 ± 2.62	7.77 ± 0.21	64.31	1.00 ± 0.22	1[b]	–
E1	12.35 ± 1.85	8.74 ± 0.12	66.18	0.54 ± 0.15	1[b]	–
			2002.77			
0	1280.01 ± 192.00	0.00	–	0.47 ± 0.14	0[c]	62.23
J	100.40 ± 15.06	0.61 ± 0.28	68.62	0.30 ± 0.12	1[b]	–
I	78.58 ± 11.79	1.30 ± 0.22	61.52	0.34 ± 0.12	1[b]	–
H	90.33 ± 13.55	2.30 ± 0.02	64.39	0.50 ± 0.14	1[b]	–
G	47.49 ± 7.12	4.16 ± 0.07	61.40	0.84 ± 0.20	1[b]	–
E4	53.64 ± 8.05	5.51 ± 0.15	63.49	0.87 ± 0.20	1[b]	–

Table 2—Continued

ID	Flux Density [mJy]	Radius [mas]	P.A.[a] [°]	FWHM [mas]	ratio	ϕ[°]
E3	13.63 ± 2.04	6.85 ± 0.28	64.21	0.84 ± 0.20	1[b]	–
E2	10.84 ± 1.63	8.51 ± 0.21	66.27	1.23 ± 0.27	1[b]	–
E1	11.31 ± 1.70	9.69 ± 0.12	62.75	1.45 ± 0.31	1[b]	–
			2003.65			
0	1046.67 ± 157.00	0.00	–	0.32 ± 0.12	0.20	74.73
X9	576.24 ± 86.44	0.36 ± 0.30	68.30	0.09 ± 0.10	1[b]	–
K	177.19 ± 26.58	0.69 ± 0.20	66.00	0.14 ± 0.10	1[b]	–
X8	66.75 ± 10.01	1.30 ± 0.30	62.77	0.17 ± 0.11	1[b]	–
J	34.80 ± 5.22	1.94 ± 0.28	63.40	0.33 ± 0.12	1[b]	–
I	21.58 ± 3.24	2.71 ± 0.22	62.07	0.51 ± 0.14	1[b]	–
H	67.76 ± 10.16	3.86 ± 0.02	62.83	0.97 ± 0.22	1[b]	–
G	64.55 ± 9.68	5.73 ± 0.07	60.73	0.59 ± 0.15	1[b]	–
E4	7.48 ± 1.12	6.46 ± 0.15	60.88	0.57 ± 0.15	1[b]	–
E3	13.78 ± 2.07	7.95 ± 0.28	65.78	1.59 ± 0.33	1[b]	–
E1	11.72 ± 1.76	10.90 ± 0.12	63.95	1.79 ± 0.37	1[b]	–
			2004.27			
0	1204.12 ± 180.62	0.00	–	0.31 ± 0.12	0.14	70.05
X10	270.09 ± 40.51	0.44 ± 0.30	68.51	0[c]	1[b]	–
L	105.50 ± 15.83	0.82 ± 0.20	69.58	0.20 ± 0.11	1[b]	–
K	38.46 ± 5.77	1.58 ± 0.20	66.52	0.41 ± 0.13	1[b]	–
J	26.88 ± 4.03	2.42 ± 0.28	63.12	0.40 ± 0.13	1[b]	–

Table 2—Continued

ID	Flux Density [mJy]	Radius [mas]	P.A.[a] [°]	FWHM [mas]	ratio	ϕ[°]
I	11.76 ± 1.76	3.36 ± 0.22	65.95	1.09 ± 0.24	1[b]	–
H3	110.03 ± 16.50	4.45 ± 0.21	63.91	0.45 ± 0.14	1[b]	–
H2	76.83 ± 11.53	4.74 ± 0.18	59.02	0.35 ± 0.12	1[b]	–
H1	26.80 ± 4.02	5.45 ± 0.24	62.26	0.82 ± 0.19	1[b]	–
G	26.20 ± 3.93	6.81 ± 0.07	61.25	1.12 ± 0.25	1[b]	–
E4	15.80 ± 2.37	6.79 ± 0.15	61.23	0.58 ± 0.15	1[b]	–
E3	5.15 ± 0.77	8.63 ± 0.28	63.85	0.75 ± 0.18	1[b]	–
E2	5.23 ± 0.78	10.21 ± 0.21	67.04	1.37 ± 0.29	1[b]	–
E1	3.92 ± 0.59	12.94 ± 0.46	64.45	0.77 ± 0.18	1[b]	–
		2004.80				
0	1590.66 ± 238.60	0.00	–	0.28 ± 0.11	0.38	66.10
N	507.49 ± 76.12	0.33 ± 0.15	61.95	0.14 ± 0.10	1[b]	–
M	294.28 ± 44.14	0.56 ± 0.15	70.23	0.22 ± 0.11	1[b]	–
L	34.00 ± 5.10	1.06 ± 0.20	65.05	0.30 ± 0.12	1[b]	–
K	15.62 ± 2.34	1.75 ± 0.20	70.84	0.38 ± 0.13	1[b]	–
J	13.76 ± 2.06	2.55 ± 0.28	66.12	0.33 ± 0.12	1[b]	–
I	20.41 ± 3.06	3.62 ± 0.22	64.10	0.62 ± 0.16	1[b]	–
H4	41.27 ± 6.19	4.93 ± 0.24	63.72	0.64 ± 0.16	1[b]	–
H3	88.46 ± 13.27	5.25 ± 0.21	62.60	0.87 ± 0.20	1[b]	–
H2	97.12 ± 14.57	5.59 ± 0.18	59.49	1.10 ± 0.24	1[b]	–
H1	13.27 ± 1.99	6.47 ± 0.24	61.41	1.82 ± 0.38	1[b]	–

Table 2—Continued

ID	Flux Density [mJy]	Radius [mas]	P.A.[a] [°]	FWHM [mas]	ratio	ϕ[°]
G	21.67 ± 3.25	7.80 ± 0.07	61.58	0.37 ± 0.12	1[b]	–
E3	4.32 ± 0.65	9.85 ± 0.28	66.41	0.97 ± 0.22	1[b]	–
E1	6.74 ± 1.01	13.19 ± 0.46	64.15	0.77 ± 0.18	1[b]	–
			2005.02			
0	1631.40 ± 244.71	0.00	–	0.24 ± 0.11	0.21	61.51
N	542.58 ± 81.39	0.31 ± 0.15	70.03	0.06 ± 0.10	1[b]	–
M	386.90 ± 58.03	0.67 ± 0.15	63.61	0.15 ± 0.10	1[b]	–
X11	187.02 ± 28.05	0.86 ± 0.30	70.85	0.20 ± 0.11	1[b]	–
L	17.02 ± 2.55	1.47 ± 0.20	67.37	0[c]	1[b]	–
K	12.09 ± 1.81	1.99 ± 0.20	68.81	0.39 ± 0.13	1[b]	–
J	16.23 ± 2.43	3.21 ± 0.28	64.59	0.99 ± 0.22	1[b]	–
I	12.46 ± 1.87	4.28 ± 0.22	64.94	0.54 ± 0.15	1[b]	–
H4	101.42 ± 15.21	5.42 ± 0.24	62.82	0.47 ± 0.14	1[b]	–
H3	58.52 ± 8.78	5.81 ± 0.21	59.93	0.39 ± 0.13	1[b]	–
H2	46.72 ± 7.01	6.18 ± 0.18	59.53	0.79 ± 0.19	1[b]	–
H1	4.59 ± 0.69	7.16 ± 0.24	61.98	0[d]	1[b]	–
G	15.88 ± 2.38	8.07 ± 0.07	61.54	0.87 ± 0.20	1[b]	–
E3	4.09 ± 0.61	10.02 ± 0.28	66.09	1.51 ± 0.32	1[b]	–
E1	5.04 ± 0.76	13.35 ± 0.46	65.18	1.28 ± 0.27	1[b]	–
			2005.73			
0	1197.32 ± 179.60	0.00	–	0.28 ± 0.11	0.30	69.16

Table 2—Continued

ID	Flux Density [mJy]	Radius [mas]	P.A.[a] [°]	FWHM [mas]	ratio	ϕ[°]
X14	480.43 ± 72.06	0.35 ± 0.30	70.12	0.12 ± 0.10	1[b]	–
X13	224.64 ± 33.70	0.67 ± 0.30	68.78	0.13 ± 0.10	1[b]	–
N	71.31 ± 10.70	1.07 ± 0.15	63.01	0.23 ± 0.11	1[b]	–
M	219.35 ± 32.90	1.86 ± 0.15	69.54	0.34 ± 0.12	0.67	41.38
L	13.95 ± 2.09	2.41 ± 0.20	65.06	0.29 ± 0.12	1[b]	–
K	4.81 ± 0.72	3.09 ± 0.20	66.29	0[c]	1[b]	–
J	12.38 ± 1.86	4.32 ± 0.28	64.25	0.78 ± 0.18	1[b]	–
I	12.70 ± 1.91	5.33 ± 0.22	64.91	0.85 ± 0.20	1[b]	–
H4	32.74 ± 4.91	6.20 ± 0.24	61.84	0.46 ± 0.14	1[b]	–
H3	38.49 ± 5.77	6.60 ± 0.21	60.79	0.53 ± 0.15	1[b]	–
H2	35.44 ± 5.32	7.21 ± 0.18	58.47	0.84 ± 0.19	1[b]	–
H1	13.71 ± 2.06	8.20 ± 0.24	63.77	0.88 ± 0.20	1[b]	–
G	5.03 ± 0.75	9.56 ± 0.07	59.78	0.52 ± 0.14	1[b]	–
E3	1.97 ± 0.30	11.42 ± 0.28	66.32	0[d]	1[b]	–
E1	4.99 ± 0.75	15.30 ± 0.46	64.80	2.10 ± 0.43	1[b]	–

[a]The PA is measured from north through east

[b]Axis ratio fixed at 1

[c]Component degenerated during the fit

[d]Resolved structure

A. The Jet Inclination Angle

The 1996 radio outburst of 3C 111 puts strong constraints on the angle to the line of sight for this source, if one assumes that a similarly bright component as E has been ejected in the counterjet, as well. Due to differential Doppler boosting, the flux ratio between jet- and counter-jet emission is

$$\frac{S_{\rm J}}{S_{\rm CJ}} = \left(\frac{1+\beta\cos\theta}{1-\beta\cos\theta}\right)^{2-\alpha} \quad . \tag{A1}$$

¿From this, it can be derived that for a given jet to counter-jet ratio $x = \frac{S_{\rm J}}{S_{\rm CJ}}$

$$\beta\cos\theta = \frac{x-1}{x+1} \quad . \tag{A2}$$

With $\alpha = 0.3$, $S_{\rm J} = 3.4\,{\rm Jy}$ (components E and F in 1997.19), $S_{\rm CJ} < 10\,{\rm mJy}$ and $\beta < 1$, one derives $\theta < 21°$. For a realistic jet speed of, e.g., $\beta = 0.956$ ($\gamma = 3.4$), we would derive an angle to the line of sight of $\theta = 19°$. An estimate close to this value can be derived from the variability Doppler factor measured by Lähteenmäki & Valtaoja (1999) and the apparent superluminal jet speed. As outlined in detail in **?**, this leads to a value of $\theta \sim 15°$.

It is important to note that this calculation implicitly assumes symmetry between the jet and counter-jet, which in projection does not have to be the case if the counter-jet is covered by an obscuring torus as it is well-established for systems at larger inclination angles (e.g., NGC 1052: see Kadler et al. (2004)). Indeed, Faraday rotation measurements towards the 3C 111 pc-scale jet (Zavala & Taylor 2002; see also Sect. 4.5) and X-ray spectral observations (Lewis et al. 2005) find evidence for substantial amounts of obscuring material. Free-free absorption could substantially lower the counter-jet radio emission and allow for larger jet angles to the line of sight.

An independent lower limit on the inclination angle of $\theta > 21°$ was given by Lewis et al. (2005) assuming that the deprojected size of the largescale 3C 111 double-lobe structure is smaller than $500h^{-1}\,{\rm kpc}$. This discrepancy implies that either 3C 111 is unusually large

Table 3: Kinematics

Component	# of epochs	μ [mas yr^{-1}]	$\beta_{\rm app}$	Peak Flux [Jy]	Ejection Epoch
B	4	1.74 ± 0.04	5.7 ± 0.1	–	1994.07 ± 0.06
C	4	1.4 ± 0.1	4.6 ± 0.3	–	1994.60 ± 0.19
E	14	1.00 ± 0.02	3.26 ± 0.07	1.46	1996.10 ± 0.03
E1	12	1.69 ± 0.04	5.5 ± 0.1	0.30	–
E2	7	1.29 ± 0.06	4.2 ± 0.2	0.13	–
E3	12	1.22 ± 0.05	4.0 ± 0.2	0.47	–
E4	7	0.86 ± 0.05	2.8 ± 0.2	0.12	–
F	4	0.64 ± 0.07	2.1 ± 0.2	1.98	1996.13 ± 0.16
G	9	1.83 ± 0.02	5.97 ± 0.07	0.24	2000.54 ± 0.03
H	4	1.73 ± 0.02	5.64 ± 0.07	0.43	2001.43 ± 0.02
H1	4	1.9 ± 0.2	6.2 ± 0.7	0.03	–
H2	4	1.71 ± 0.11	5.6 ± 0.4	0.10	–
H3	4	1.5 ± 0.1	4.9 ± 0.3	0.11	–
H4	3	1.3 ± 0.2	4.2 ± 0.7	0.10	–
I	6	1.3 ± 0.1	4.2 ± 0.4	0.08	2001.77 ± 0.21
J	6	1.2 ± 0.1	3.9 ± 0.3	0.10	2002.30 ± 0.24
K	5	1.1 ± 0.1	3.6 ± 0.7	0.18	2003.08 ± 0.22
L	4	1.1 ± 0.2	3.6 ± 0.7	0.11	2003.74 ± 0.22
M	3	1.5 ± 0.2	4.9 ± 0.7	0.39	2004.50 ± 0.12
N	3	0.9 ± 0.2	2.9 ± 0.7	0.54	2004.57 ± 0.19

or there is a misalignement between the large-scale jet-axis and the parsec-scale jet axis inclination to the line of sight, while the projected position angles of the large-scale jet (63°) and the parsec-scale jet ($\sim$ 65°) more or less match.

B. Image-Plane vs. (u, v)-plane Model Fitting

It is interesting to compare our results from this very detailed analysis of one individual object with the results of the kinematical-survey analysis of Kellermann et al. (2004), who investigated the speeds of 110 extragalactic jets, including 3C 111, based on the VLBA 2 cm Survey data between 1995 and 2001. Kellermann et al. (2004) performed the component identification in the image plane and represented the evolving structure of component E and its trailing features via one component. In total, they consider three moving components: between 1995 and 1996, Kellermann et al. (2004) identify two components between 1 mas and 5 mas from the core to which they assign a "poor" quality code. In this work, this region has been represented by four different components (A, B, C, D) of which two (B, C) could be traced over four epochs and the model fitting was done in the (u, v)-domain. We find $(5.7 \pm 0.1)c$ and $(4.6 \pm 0.3)c$ for components B and C while Kellermann et al. (2004) report $(4.2 \pm 1.0)c$ and $(2.9 \pm 1.7)c$. While we believe that, in the framework of our overall kinematical model, the representation of this region with four different components is the most consistent one, it needs to be noted that the 1995/1996 data do not fully constrain any multi-epoch model, so that the differences between this work and Kellermann et al. (2004) in this range should not be over-interpreted. More insightful is the comparison of our model of the post-1996 ejecta, involving the components E, F, E1, E2, E3, and E4, with the one component that Kellermann et al. (2004) used to represent this structure, which is assigned an "excellent" quality code and which is found to travel with a speed of $(4.9 \pm 0.2)c$ along the jet. Formally, this speed is in remarkable agreement with the

speed of our leading component E1 so that it has to be concluded that the much simpler model derived from image-plane analysis well represented the fastest moving structure. The acceleration (with respect to the ejecta's smaller velocity prior to mid 1999), as well as the additional components that we interpret as a backward shock and trailing jet features do become visible only after a more complicated model fitting of the data in the (u, v)-domain. The necessarily less-complex model used in a survey analysis like the one conducted by Kellermann et al. (2004) is only part of the reason for this discrepancy. Image-plane analysis makes it very difficult to interpret a moving feature that changes it's structure in a complex way and that has no clear persistent brightness maxima. In addition, (u, v)-plane fitting in general achieves higher angular resolution so that the two bright, but closely separated components E and F could not be distinguished in in early to mid 1996. Figure 11 demonstrates that even in October 1996 when E and F are separated by only 0.3 mas and are located within 1 mas from the core, a one-component model clearly fails to represent this compact structure.

We would like to acknowledge the support of the rest of the MOJAVE Team, who have contributed to the data used in this paper, in particular we would like to thank Christian Fromm for his help with the production of the figures for the paper. We are grateful to Greg Taylor, who provided complementary 2 cm VLBA data for an additional epoch. The MOJAVE project is supported under National Science Foundation grant 0406923-AST. The Very Long Baseline Array is operated by the National Radio Astronomy Observatory, a facility of the National Science Foundation operated under cooperative agreement by As- sociated Universities, Inc. MK has been supported in part by a Fellowship of the International Max Planck Research School for Radio and Infrared Astronomy and in part by an appointment to the NASA Postdoctoral Program at the Goddard Space Flight Center, administered by Oak Ridge Associated Universities through a contract with NASA.

REFERENCES

Agudo, I., Gómez, J., Martí, J. M., et al. 2001, ApJ, 549, L183

Alef, W., Preuss, E., Kellermann, K. I., Gabuzda, D., 1998, in Radio Emission from Galactic and Extragalactic Compact Sources, ASP Conf. Ser. 144, 129

Aller, M. F., Aller, H. D., Hughes, P. A., 2003, in Radio Astronomy at the Fringe, Zensus, J. A., Cohen, M. H., Ros, E. (eds.), ASP Conference Ser. 300, 159

Aloy, M.-Á., Martí, J.-M., Gómez, J.-L., Agudo, I., Müller, E., & Ibáñez, J.-M. 2003, ApJ, 585, L109

Cara, M., & Lister, M. L. 2007, ArXiv Astrophysics e-prints, arXiv:astro-ph/0702449

Cohen, M. H., Lister, M. L., Homan, D. C., Kadler, M., Kellermann, K. I., Kovalev, Y. Y., & Vermeulen, R. C. 2007, ApJ, 658, 232

Goetz, M. M. A., Preuss, E., Alef, W., & Kellermann, K. I. 1987, A&A, 176, 171

Gómez, J., Marscher, A. P., Alberdi, A., Jorstad, S. G., Agudo, I. 2001, ApJ, 561, L161

Hartman, R. C., et al. 1999, ApJS, 123, 79

Hartman, R. C. & Kadler, M. 2007, ApJ, submitted

Homan, D. C., et al. 2006, ApJ, 642, L115

Jorstad, S. G., Marscher, A. P., Lister, M. L., et al. 2005, AJ, 130, 1418

Kadler, M., 2005, Ph. D. Thesis, Rheinische Friedrich-Wilhelms-Universität Bonn, Bonn, Germany

Kadler, M., Ros, E., Lobanov, A. P., Falcke, H., Zensus, J. A. 2004, A&A, 426, 481

Kellermann, K. I., Vermeulen, R. C., Zensus, J. A., & Cohen, M. H. 1998, AJ, 115, 1295

Kellermann, K. I., Lister, M. L., Homan, D. C., et al. 2004, ApJ, 609, 539

Kharb, P., Gabuzda, D., Alef, W., Preuss, E., & Shastri, P. 2003, New Astronomy Review, 47, 621

Kovalev, Y. Y., Kellermann, K. I., Lister, M. L., et al. 2005, AJ, 130, 2473

Lähteenmäki, A. & Valtaoja, E. 1999, ApJ, 521, 493

Lewis, K. T., Eracleous, M., Gliozzi, M., et al. 2005, ApJ, 622, 816

Linfield, R. & Perley, R. 1984, ApJ, 279, 60

Lister, M. L., & Homan, D. C. 2005, AJ, 130, 1389

Mukherjee, R., Halpern, J., Mirabal, N., & Gotthelf, E. V. 2002, ApJ, 574, 693

Perucho, M., Agudo, I., Kadler, M., Ros, E., Kovalev, Y. Y., 2007, ApJ, in prep.

Perucho, M., & Lobanov, A. P., 2007, A&A, 469, L23

Perucho, M., Hanasz, M., Martí, J.M., Miralles, J.A., 2007, Phys. Rev. E, 75, 056312

Preuss, E., Alef, W., Kellermann, K.I. 1988, IAU Symp. 129: The Impact of VLBI on Astrophysics and Geophysics, 105

Sguera, V., Bassani, L., Malizia, A., Dean, A. J., Landi, R., & Stephen, J. B. 2005, A&A, 430, 107

Sreekumar, P., Bertsch, D. L., Hartman, R. C., Nolan, P. L., & Thompson, D. J. 1999, Astroparticle Physics, 11, 221

Teräsranta, H., Achren, J., Hanski, M., et al. 2004, A&A, 427, 769

Tingay, S. J., Preston, R. A., & Jauncey, D. L. 2001, AJ, 122, 1697

Zavala, R. T., & Taylor, G. B. 2002, ApJ, 566, L9

Zensus, J. A., Ros, E., Kellermann, K. I., et al. 2002, AJ, 124, 662

This manuscript was prepared with the AAS LaTeX macros v5.2.